Full Paper

Propellants, Explosives, Pyrotechnics

DOI: 10.1002/prep.201300154

# Factors Influencing Temperature Fields during Combustion Reactions

**Keerti Kappagantula,[a] Charles Crane,[b] and Michelle Pantoya*[a]**

**Abstract**: A unique, non-invasive diagnostic technique for characterizing two-dimensional thermal fields generated during the combustion of nanothermites was developed. Temperature resolved thermal images of the reactions were obtained using infrared imaging coupled with multiwavelength pyrometry. Thermal images of fuel rich aluminum/copper oxide (Al/CuO) and aluminum/polytetrafluoroethylene (Al/PTFE) mixtures embedded with different additives were analyzed and the principal factors affecting the spatial distribution of temperature during their combustion were identified. Results showed two distinct temperature zones during combustion: a hot zone surrounding the point of ignition, where the highest temperatures were recorded followed by a lower temperature region called the intermediate zone. Temperatures are plotted as a function of distance from the point of ignition such that inflection points distinguishing temperature gradients provide an indication of the range of the thermal influence. Gas generation and heat of combustion are principal factors affecting temperature fields: greater gas generation in addition to condensed phase products promotes higher temperatures in the far field. Results also indicate that faster reactions attain higher temperatures and more extensive temperature fields. This observation is attributed to greater momentum of the gas and condensed phase products projected from the hot zone that shift the inflection point farther. These results show that multiphase convection is a governing mechanism promoting thermal energy distributions.

**Keywords:** Thermites · Nanoparticle combustion · Aluminum · Infrared thermometry · Non-ideal explosives

## 1 Introduction

This last century saw a push towards understanding and developing energetic materials, with some emphasis to their application in the ordnance sector. Particular characteristics of interest are ignition sensitivity, energy release rate and reaction temperature of candidate formulations. As demand propelled towards faster and more energy dense materials, effort focused on increasing the impulsive loading and thermal extent of energetic formulations, including pyrotechnics, explosives, and propellants. One approach was to add particulate media to conventional high explosives resulting in heterogeneous explosives. The particulate additives introduced into the explosive charges may participate in the combustion reaction [1–5] or remain unreactive [6, 7]. Upon ignition heterogeneous explosives give rise to an outward moving blast wave that attenuates due to the effects of spreading; simultaneously, solid particles pick up momentum from the combustion gases and propagate in the blast wave [8]. The solid particles in the blast wave contribute to heat transfer from the reaction and increase the far-field temperatures [9].

When reactive particles like metals are added to the explosive charge, the particle size can impact the formulation performance. Fine particles react rapidly but limit the degree of reaction due to insufficient oxidizers in the explosive system. On the other hand, large particles may not ignite if the explosive residence times are too short, although these particles are dispersed widely following thermal initiation of the charge [9]. So, there exists a critical particle size that can be added to a high explosive charge in order to optimize thermal effects from the blast wave. Yet, there are many parameters that control this optimization that are coupled such as gas generation, stoichiometry, calorific output, and reaction rate. The mechanisms promoting energy dispersion are a function of these parameters. The challenge is to tailor reactants toward specific reaction outputs but monomolecular explosives have limited tailorability. What is needed is a better understanding of the influence of the different parameters on energy dispersion during reaction and to exploit these parameters, but that is not easily achieved when using homogeneous monomolecular explosives with our without additives.

[a] *K. Kappagantula, M. Pantoya*
*Department of Mechanical Engineering*
*Corner of 7th and Boston Avenue*
*Texas Tech University*
*Lubbock, Texas. 79409 USA*
**e-mail: michelle.pantoya@ttu.edu*

[b] *C. Crane*
*Los Alamos National Laboratory*
*4200 W Jemez Rd #300*
*Los Alamos, NM 87544, USA*

  

With the advent of nanotechnology, a new genre of reactive energetic materials known as nanothermites, nanoenergetics [10], metastable intermolecular composites (MICs) [11], superthermites [12], and pyrolants [13] have been gaining popularity in ordnance applications [14]. All of these names describe a class of composite materials (nanothermite) comprised of a metallic fuel and organic or metallic oxidizer and will be referred to as nanothermites hence forth. The most common fuel used is aluminum (Al) due to its high heat of combustion in an oxygen environment (ca. 32 $kJ\,g^{-1}$) [8]. The significance of using nano Al instead of μm-sized Al is that a reduction in the size results in an increase in the ignition sensitivity and reaction rates by several magnitudes [15,16]. There is no profound thermodynamic advantage in using nanomaterials; however, whereas micrometer size energetic formulations are harder to initiate and slower to propagate, nanoparticles require less ignition energy and are more dispersive (e.g., because of the lighter individual particles). These attributes have spurred new interest in developing nanoparticle reactive materials, which may achieve tailorability and performance surpassing homogeneous explosives. This is be evidenced by their varied and diverse applications [17–24].

Despite the widespread nanothermite research, surprisingly little is reported on actual measurements of flame temperature and even less on temperature fields generated during combustion. Harnessing the thermal energy from these reactions is fundamentally important for any energy generation application and knowledge of the temperature fields generated gives insight into the thermal effects, particle dynamics and combustion processes involved. Additionally, selecting a reactant formulation tailored toward enhanced temperature distributions would require an understanding of the mechanisms that propagate energy during a nanothermite reaction.

A review of the recent work in nanothermite temperature measurement techniques and advances is provided in Ref. [25]. Optical pyrometry has become the preferred tool in measuring high temperatures generated during nanothermite combustion. This technique uses continuous spectra emitted by the condensed reaction products to determine their temperature. In addition, infrared (IR) thermometry has been used to measure temperatures in the highly evolving, harsh environment of combustion reactions [9,26]. Although there is a balance between the resolution of the temperature field and the area that can be monitored by the camera, with the development of advanced diagnostics for IR radiometry like high resolution high-speed IR cameras, this technique has become one of the favored noninvasive measurement methods. However, one of the major drawbacks of IR thermometry is that calculations of temperature require an estimation of emissivity, which can be complex within the multi-phase, multi-component, highly turbulent fluid fields of a reaction. Thus, IR thermometry is a useful temperature measurement technique *only if* there is a good estimate of the emissivity associated with the reacting media [27].

Apart from experimentally obtained data, thermoequilibrium modeling software such as REAL or CHEETAH predict the temperatures generated during nanothermite combustion [28]. The models are limited by equilibrium assumptions under either a constant pressure or volume condition with no energy loss and are not representative of high heating rates associated with in-situ combustion or consider the extent of reaction completion which can be correlated to particle size of the reactants as well as other reactant properties. However, the models are useful and provide a qualitative comparison between candidate formulations for a particular application.

In order to understand the complex thermal effects of nanothermites during their combustion, a unique diagnostic approach was recently developed that measures the temperature fields from nanothermite reactions [25]. Point source temperature measurements of a reaction are obtained from a five channel multi wavelength radiometer and coupled with thermal images from an IR camera to calculate the thermal emissivity of aluminum (Al) and polytetrafluoroethylene (PTFE) reaction and thus determine its two-dimensional (2D) temperature field. The objective of this study is to utilize this new diagnostics technique to measure the temperature field generated for two different nanothermite reactions: one composed of Al and PTFE; and the other composed of Al and copper oxide (CuO). These base reactions differ significantly in their gas generation behaviors that contribute toward affecting far field temperatures. In addition to these base formulations, metal and metal oxide nanoparticles were incorporated as additives to alter the temperature fields either through producing additional condensed phase products or through secondary reactions. The reactions are also modeled using REAL in order to obtain an estimate of their heats of combustion and percent of gas generated on combustion. Possible correlations existing between temperature fields and parameters such as additive, heat of combustion, and gas generation are examined.

## 2 Experimental

Aluminum with an average particle diameter of 80 nm encapsulated in an $Al_2O_3$ shell (of average thickness 2.7 nm) was used as the fuel. Polytetrafluoroethylene (PTFE) and copper oxide (CuO) were used as oxidizers, and combined with Al to yield Al/PTFE and Al/CuO, respectively. The two oxidizers were selected for their distinctive characteristics: Al/PTFE generates a lot of gas phase products, while Al/CuO generates comparatively less gas and more condensed phase products. Different metals and metal oxides were added to the base nanothermite in order to determine the additives' influence on the temperature fields generated. Table 1 provides details of all the materials (additives, fuel, oxidizers).

  

**Table 1.** Material details including supplier and average particle diameter.

| Material | Supplier | Average particle diameter |
|---|---|---|
| Aluminum (Al) | Novacentrix | 80 nm |
| Polytetrafluoroethylene (PTFE) | Dupont | 200 nm |
| Copper(II) oxide (CuO) | Sigma Aldrich | 50 nm |
| Manganese(IV) oxide ($MnO_2$) | Alfa Aesar | 44 μm |
| Molybdenum(VI) trioxide ($MoO_3$) | Nanostructured and Amorphous Materials, Inc. | 370 nm |
| Tungsten(VI) trioxide ($WO_3$) | Nanomat, Inc. | 50 nm |
| Boron (B) | Alfa Aesar | 20 nm |
| Iron (Fe) | Alfa Aesar | 30 nm |
| Magnesium (Mg) | Alfa Aesar | 44 μm |
| Manganese (Mn) | Alfa Aesar | 40 nm |
| Titanium (Ti) | Sigma Aldrich | 44 μm |

**Table 2.** Weight percentages of the reactants and the corresponding equivalence ratios used to synthesize nanothermites.

| Nanothermite | ER | Al [% weight] | Oxidizer [% weight] |
|---|---|---|---|
| Al/CuO | 1.1 | 24.90 | 75.10 |
| Al/PTFE | 1.4 | 39.86 | 60.14 |

During sample preparation, the equivalence ratio (ER) of Al/PTFE and Al/CuO was maintained at 1.4 and 1.1, respectively. The weight percentages of the reactants used to achieve these ERs are shown in Table 2. The detailed nanothermite synthesis technique is given elsewhere [25] and is summarized herein. Reactant powders were combined with hexanes and sonicated for 60 s to produce improved homogeneity. The suspension was transferred into a Pyrex dish under a fume hood to evaporate the hexane. The dried powders were reclaimed for further experimentation.

Copper oxide (CuO), manganese oxide ($MnO_2$), molybdenum trioxide ($MoO_3$), and tungsten trioxide ($WO_3$) were added to Al/PTFE at 10% weight of the nanothermite sample. They were added to Al/PTFE to study the effects of additives altering the gas generation and temperature fields. Similarly, in order to study the temperature fields altered due to presence of different kinds of fuels as additives, boron (B), iron (Fe), magnesium (Mg), manganese (Mn), and titanium (Ti) nanoparticles were added to Al/CuO at 10% by weight of the nanothermite sample. The nanothermites with the additives will be referred to using the nomenclature "fuel/oxidizer/additive" henceforth. For example, Al/CuO containing 10% by weight of Mg will be referred to as Al/CuO/Mg.

Experiments were conducted to determine the temperature fields during a reaction. Phase I consisted of obtaining point source temperatures of unconfined reactions using a five channel radiometer. Phase II involved thermal imaging of the reactions in a 3.5 cm × 8 cm field of interest, using a 14-bit, high speed midwave (3–5 μm) IR camera with an indium antimonide (In-Sb) detector (FLIR Systems). Phase III focused on coupling the radiometer data with the thermal imaging data using an infrared (IR) camera to resolve a spatial and temporal distribution of temperature during the reaction. Detailed description of the apparatus and procedure used to determine the temperature field is given elsewhere and summarized below [25]. In addition to these experiments, the reactions were modeled as open systems at constant atmospheric pressure, using REAL, a thermal equilibrium software package, to aid in understanding underlying mechanisms associated with experimental observations.

### 2.1 Phase I: Radiometer Experiments

Figure 1 shows the setup for the temperature measurement experiments using the radiometer. The sample was placed on a pedestal, surrounded by thermal shields for safety. A five-channel radiometer was used for point source temperature measurements. On ignition by nichrome wire, the five photodetectors in the radiometer detect light from the thermal event. Table 3 shows the central wavelength and the band widths of the five photodetectors of the radiometer. Ratios of the signals from the photodetectors were taken, which when combined with the calibration data, were used to find ten temperature profiles of the thermal event from the reaction as a function of time. The temperatures from the ten profiles, averaged, for each point of time were considered to be the temperature as a function of time. Based on the theory of pyrometry, the radiometer calculates temperature proportional to the intensity of the irradiation detected by it. In order to determine the maximum temperature during the nanothermite reaction, the time frame at which the radiometer detected the maximum light intensity from the combustion reaction was identified. The average temperature corresponding to this intensity at that time was denoted as the maximum temperature ($T_{max}$) of the nanothermite reaction.

Seven tests were conducted for each sample to monitor repeatability. During experimentation, care was taken to reduce thermal emission and reflection from all the surfaces of the apparatus. The shields and the pedestal were painted black. The experimental setup was also isolated

  

Propellants, Explosives, Pyrotechnics

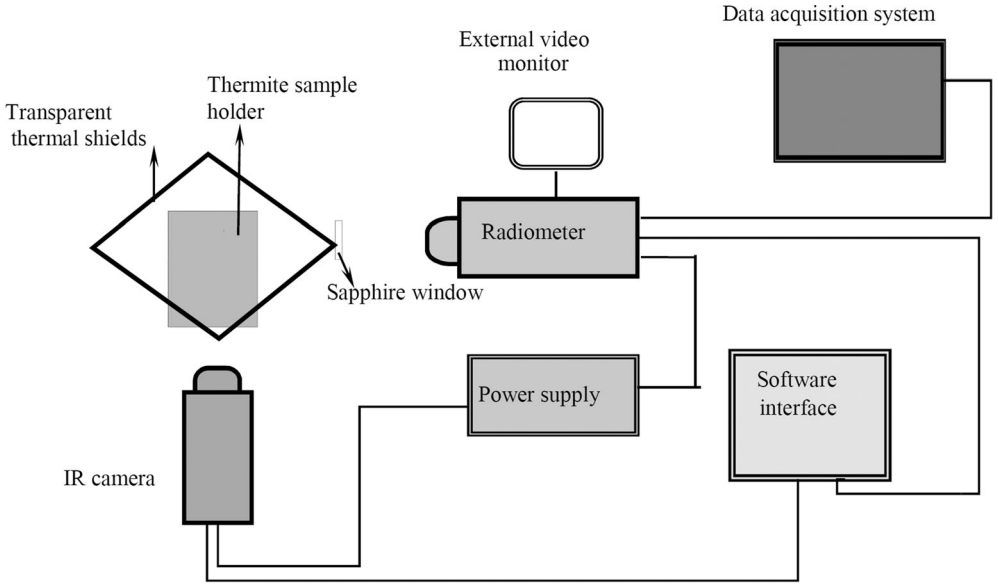


**Figure 1.** Schematic of the radiometer apparatus used for measuring sample temperature.

**Table 3.** Central wavelength and band width of the five channel radiometer photodetectors.

| Channel number | Central wavelength [nm] | Band width [nm] |
|---|---|---|
| 1 | 900 | 10 |
| 2 | 1150 | 10 |
| 3 | 1535 | 90 |
| 4 | 1982 | 87 |
| 5 | 2600 | 35 |

from sources of thermal radiation and stray light that can decrease the signal-to-noise ratio.

### 2.2 Phase II: IR Imaging

Figure 1 also shows the schematic of the apparatus used for obtaining thermal images of the reaction. The sample was placed over a nichrome wire attached to an acrylic plate that was painted black. The plate was placed in a volume formed by four transparent shields. The IR camera was placed at a distance of 68 cm from the sample. The location of the camera remained constant throughout the duration of the experiments. The IR camera records at a sample rate of 402 Hz with an integration time of 0.28 μs. A Mikron M300 blackbody with an effective emissivity of $+0.995$, temperature range of 200–1150 °C, and an accuracy of 0.25 % of the reading $\pm 1$ K was used to calibrate the IR camera. Light emitted by the sample on its ignition was intercepted by the camera in the form of analog/digital (AD) count. This data was converted into thermal radiance values ($R$) by the IR camera software and imaged by comparing it to the blackbody calibration. It was assumed that thermal radiation absorption from the environment was negligible and did not interfere with the thermal imaging.

### 2.3 Phase III: Coupling Pyrometer and IR Data

For each nanothermite, the thermal image with the maximum amount of radiance was identified. From each of these identified thermal images, the maximum thermal radiance value and its location were identified. This location was also the location of the maximum temperature, according to the theory of radiometry [25]. Thus, the temperature of this point was identified as $T_{max}$ (measured by the radiometer) for the corresponding reaction. Therefore, a thermal image of the reaction with the maximum temperature value and its location was obtained at the instant when it recorded its maximum thermal radiance. However, the temperature values elsewhere in the image were still unknown. To determine these, the emissivity ($\varepsilon$) of the material needed to be determined at that instant of time when the reaction reached its maximum temperature ($T_{max}$). This was computed using Planck's equation for band emission (with $T = T_{max}$).

$$\varepsilon = \frac{\pi R}{\int_0^5 \frac{c_{1L}}{\lambda^5\left(e^{c_2/\lambda T}-1\right)}d\lambda - \int_0^3 \frac{c_{1L}}{\lambda^5\left(e^{c_2/\lambda T}-1\right)}d\lambda} \quad (1)$$

In Equation (1), $\varepsilon$ is the emissivity of the nanothermite, $R$ is the radiance measured by the IR camera, $c_{1L}$ and $c_2$ are the first and second radiation constants respectively. This $\varepsilon$ was integrated into a fourth degree polynomial, shown as Equation (2) obtained from the calibration data of the IR camera along with the radiance values recorded by it.

  

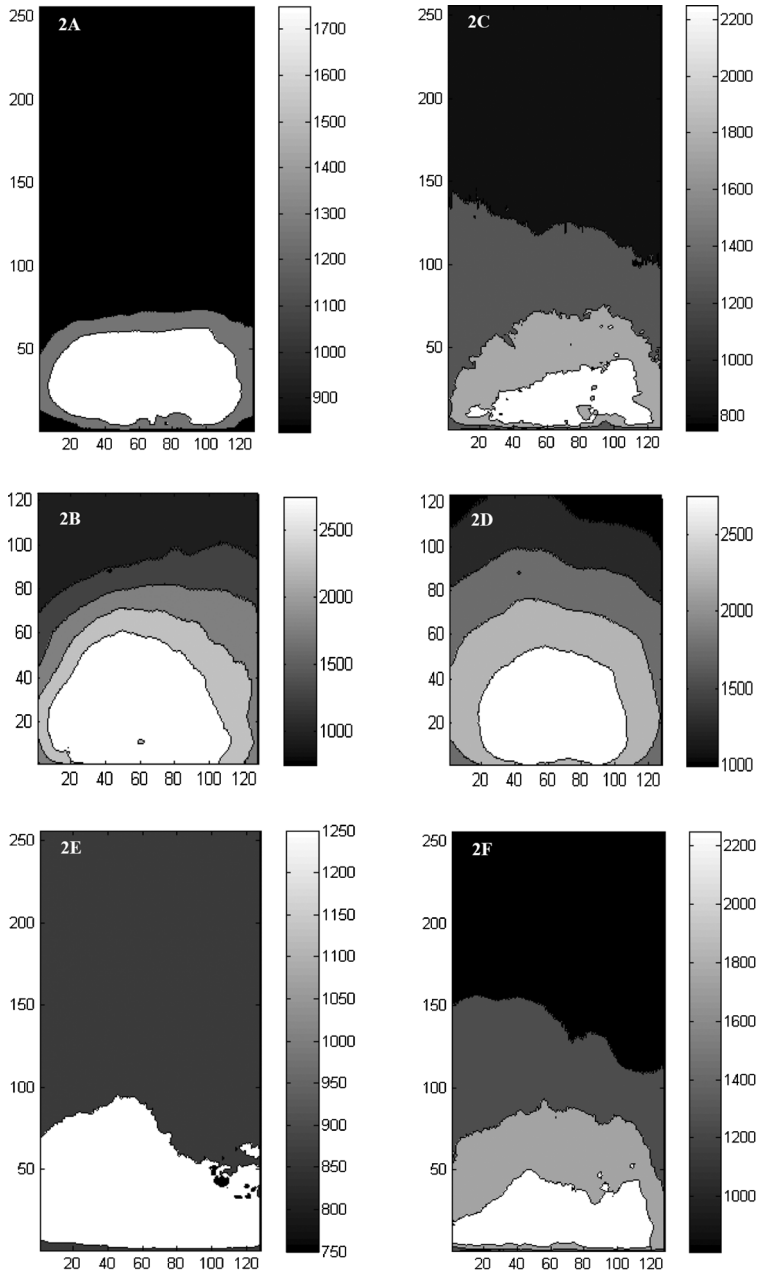


**Figure 2.** Thermal images of (A) Al/CuO, (B) Al/CuO/B, (C) Al/CuO/Fe, (D) Al/CuO/Mg, (E) Al/CuO/Mn, and (F) Al/CuO/Ti.

$$-0.01809\left(\frac{R}{\varepsilon}\right)^4 + 0.85397\left(\frac{R}{\varepsilon}\right)^3 - 15.66940\left(\frac{R}{\varepsilon}\right)^2 + 277.07110\left(\frac{R}{\varepsilon}\right) + 623.4434 = T \quad (2)$$

Each location in the thermal image recorded at the instant of $T_{max}$ has a unique radiance value, which when combined with $\varepsilon$ using Equation (2), yielded the temperature of that unique location. Thus, the temperature at each location was then calculated and this enabled a 2D mapping of the temperature field at the time when the maximum temperature was reached by the reacting nanothermite [25].

The temperatures in the field of interest along a vertical axis (passing through the point of maximum temperature) were plotted as a function of distance away from the point of ignition to obtain the temperature profiles of the various reactions. In order to compare the experimental results obtained with theoretical equilibrium reaction calculations, the adiabatic flame temperatures ($T_{ad}$), heat of combustion, and products generated for the different reactions were simulated using REAL code.

One of the primary factors for measuring the temperature, as enumerated before, is the emissivity of the reacting nanothermite. The emissivity of a material depends on the duration of emission, properties of the material emitting,

  

wavelength of emission and temperature at which the material is emitting, among others. During nanothermite synthesis, the reactants were thoroughly mixed such that the existence of density gradients may be decreased greatly. In addition, the environment in which the testing took place was kept free of turbulence inducing mechanisms to ensure quiescence, thus not leading to the mixing of the products formed and air. These measures may ensure homogeneity of the products formed and the possibility of intermixing of air and the combustion gases. Also, the temperature fields were estimated for only one thermal image implying the independence of time and emissivity. Thus, taking all these factors into consideration, the current study was based on the assumption that the combustion gas cloud generated during nanothermite combustion is fairly homogeneous and does not have emissivity varying significantly over the field of view of the camera.

## 3 Results

Figure 2A–F and Figure 3A–E show thermal images for Al/CuO and Al/PTFE without and with additives, respectively. Each change in color corresponds to a temperature gradation of 750 K.

The temperature along the vertical axis passing through the point of ignition as a function of distance is shown for each corresponding thermal image in Figure 4A,B and Figure 5A,B. These thermal profiles may be used to assess the temperature distribution in the field of interest. For example, a steeper temperature gradient indicates a quicker loss of heat to the surroundings.

Maximum reaction temperatures ($T_{max}$) recorded by the five channel multi wavelength radiometer are given in Table 4 along with time to reach $T_{max}$. Also included in Table 4 are simulation results for heats of combustion, $T_{ad}$ and percent of gas phase products.

The temperature fields generated have two distinct zones: the *hot zone* i.e., where the highest temperatures are recorded and the *intermediate zone*, with temperatures

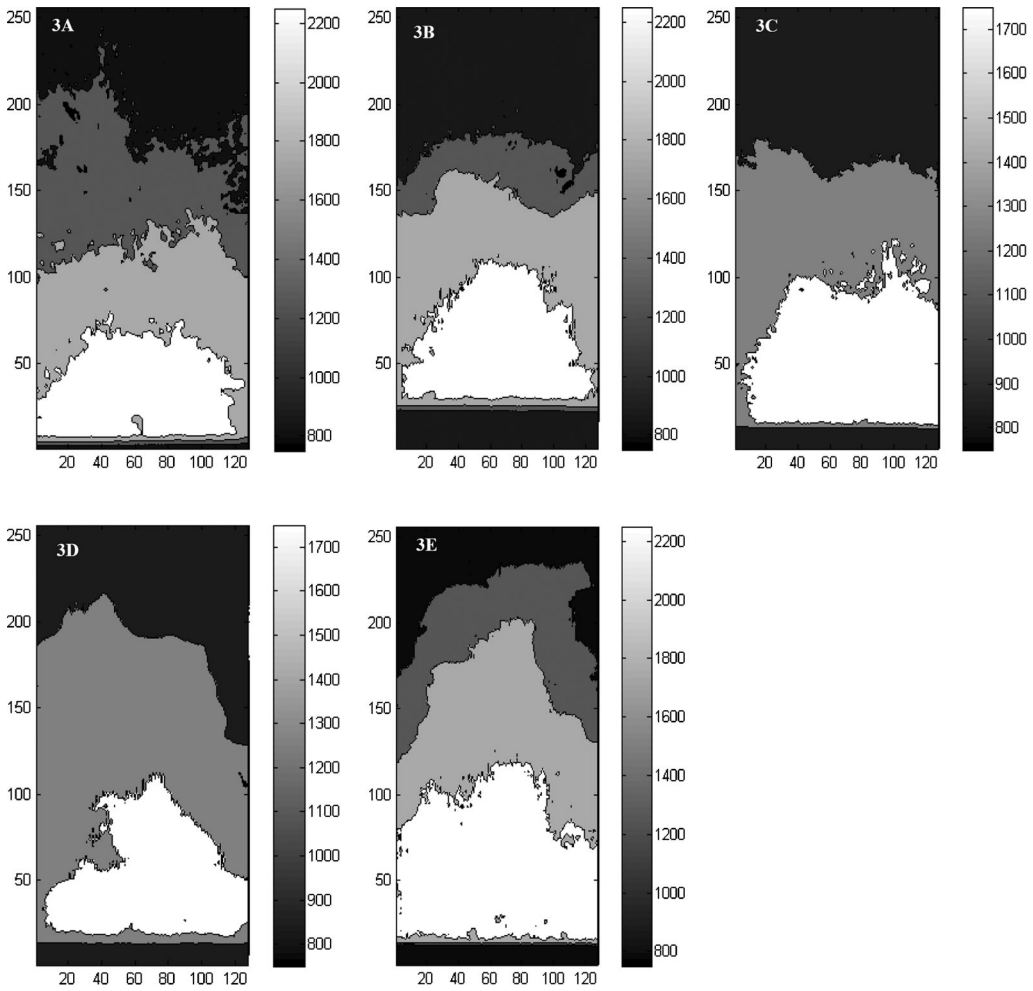


**Figure 3.** Thermal images of (A) Al/PTFE, (B) Al/PTFE/CuO, (C) Al/PTFE/$MnO_2$, (D) Al/PTFE/$MoO_3$, and (E) Al/PTFE/$WO_3$.

  

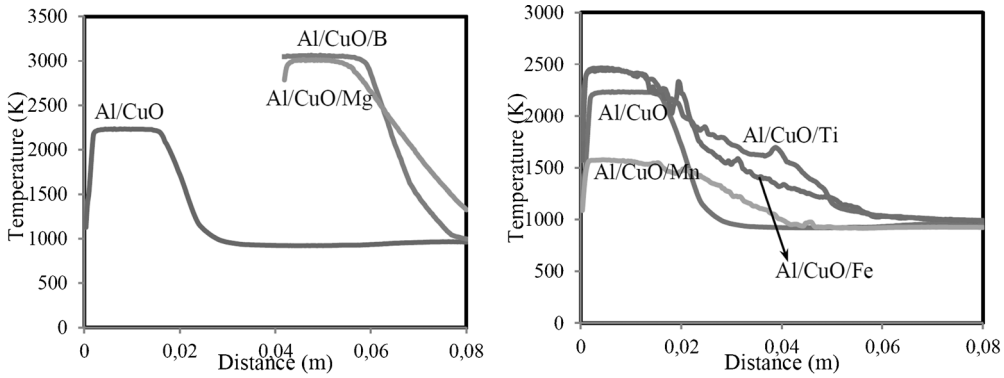


**Figure 4.** Temperature profiles of (A) Al/CuO/B, Al/CuO/Mg and (B) Al/CuO/Fe, Al/CuO/Mn, Al/CuO/Ti. Temperature profile of AC is provided in both the plots for reference.

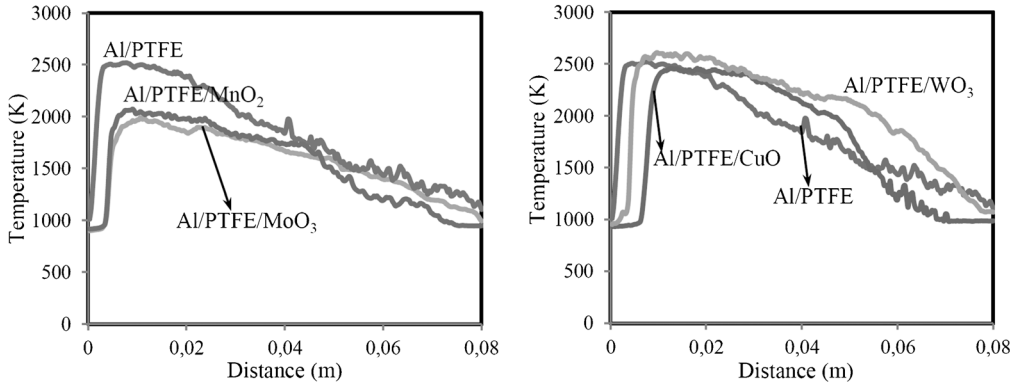


**Figure 5.** Temperature profiles of (A) Al/PTFE/$MnO_2$, Al/PTFE/$MoO_3$ and (B) Al/PTFE/CuO, Al/PTFE/$WO_3$. Temperature profile of Al/PTFE is provided in both the plots for reference.

**Table 4.** Summary of results.

| Nanothermite | $T_{max}$ [K] | $T_{ad}$ [K] | Heat of combustion [kJ kg$^{-1}$] | Product gases generated [%] | Location of inflection point [m] | Time to $T_{max}$ from ignition [ms] |
|---|---|---|---|---|---|---|
| Al/CuO | 2234 | 2987 | 3786 | 29 | 0.0156 | 2.7 |
| Al/CuO/B | 3065 | 3181 | 3478 | 14 | 0.0562 | 0.9 |
| Al/CuO/Fe | 2450 | 2923 | 3441 | 23 | 0.0122 | 5.0 |
| Al/CuO/Mg | 3017 | 3166 | 3640 | 26 | 0.0534 | 1.7 |
| Al/CuO/Mn | 1581 | 2686 | 3442 | 27 | 0.0212 | 4.9 |
| Al/CuO/Ti | 2464 | 2703 | 3442 | 28 | 0.0137 | 3.3 |
| Al/PTFE | 2519 | 3341 | 7672 | 86 | 0.0131 | 48.1 |
| Al/PTFE/CuO | 2458 | 3022 | 7394 | 83 | 0.0465 | 64.6 |
| Al/PTFE/$MnO_2$ | 2072 | 2715 | 7544 | 81 | 0.0462 | 61.3 |
| Al/PTFE/$MoO_3$ | 1991 | 3047 | 7425 | 88 | 0.0493 | 113.8 |
| Al/PTFE/$WO_3$ | 2611 | 3112 | 7191 | 89 | 0.0484 | 64.6 |

lower than those recorded in the hot zone but significantly higher than the room temperature. The temperature profiles distinguish these two regions by a sharp change in the slope; temperatures in the intermediate region decline at a faster rate compared to those in the hot region. The points on the temperature profiles in Figure 4 and Figure 5 where the slope shifts from gradual (in the hot region) to steep (in the intermediate region) is distinctive on all temperature profiles and is defined as the *inflection point*. Table 4 shows the vertical distance of the inflection point from the sample holder, for each nanothermite.

  

Figure 2 and Table 4 show that the introduction of B and Mg as additives increases the $T_{max}$ of Al/CuO, whereas addition of Fe and Ti does not change the maximum temperature significantly. However, Fe and Ti serve to push the inflection points farther out as is seen from Figure 4B. Only the addition of Mn to Al/CuO reduces its maximum temperature and gives lower values of temperature away from the point of ignition in the temperature field.

Table 4 shows the time taken for each nanothermite to attain the corresponding $T_{max}$. While the addition of Fe, Mn, and Ti to Al/CuO increases the time to $T_{max}$, adding B and Mg reduces it. A point of interest is the location of the temperature profiles of Al/CuO/B and Al/CuO/Mg as well as their inflection points compared to that of Al/CuO (0.056, 0.053, and 0.015 m, respectively). Since the time taken to $T_{max}$ was much smaller for Al/CuO/B and Al/CuO/Mg than that of the other nanothermites, the resolution of the IR camera was not sufficient to obtain the thermal image when the Al/CuO/B and Al/CuO/Mg attained their respective $T_{max}$. In order to increase the resolution of the hot zone while effectively capturing the spatial distribution, the field of interest was reduced to 3.5 cm × 4 cm and was confined to 4 cm above ignition since that was the area that had the location of $T_{max}$ and maximum gas contribution as seen in the initial experiments. This is the reason temperature profiles in Figure 4A for Al/CuO/B and Al/CuO/Mg span only from 0.04 m to 0.08 m.

As seen from Table 4 and Figure 3, the maximum temperatures recorded when $MnO_2$ and $MoO_3$ are introduced into Al/PTFE (Figure 3C and D) are much lower than those of Al/PTFE (Figure 3A); whereas addition of $WO_3$ increases the maximum temperature of the Al/PTFE reaction (Figure 3B). The thermal images show that almost same temperatures are sustained spatially with $WO_3$ and CuO as additives to Al/PTFE compared to Al/PTFE. On the other hand, thermal images of Al/PTFE/$MnO_2$ and Al/PTFE/$MoO_3$ yield lower temperatures spatially with respect to Al/PTFE. Figure 5A,B and Table 4, however, show that the inflection points for Al/PTFE with oxide additives are located farther in the field of interest than that of the Al/PTFE reaction alone. It should also be noted that the time to $T_{max}$ for all the Al/PTFE nanothermites with additives is more than Al/PTFE reaction alone (see Table 4).

Table 4 shows $T_{ad}$ calculated theoretically. It should be noted that the reaction mechanisms for the equilibrium conditions and actual runaway reactions are entirely different. Thermoequilibrium conditions, which are employed to obtain the $T_{ad}$, imply that the reactions have very slow, controlled heating rate which is not the case with the real-time nanothermite reactions. Experimentally obtained $T_{max}$ values from the radiometer correspond to nanothermites with very fast heating rate and non-equilibrium conditions. Also, $T_{ad}$ is modeled for adiabatic conditions, whereas the actual experiments are performed in an open environment, implying that the comparison between $T_{max}$ and $T_{ad}$ will not be very close. Therefore, the $T_{ad}$ of the nanothermites, modeled for equilibrium conditions, may be used as a reference or guideline in order to understand the different factors that affect the spatial distribution of temperature.

## 4 Discussion

### 4.1 Al/CuO with Metal Additives

More than 80 % of the combustion products of Al/PTFE are in the gas phase. Correspondingly, the far field temperatures measured in the intermediate region for Al/PTFE are higher than Al/CuO. These results indicate that an important mechanism controlling the location of the inflection point is convective and the phase of the products. Gas and condensed phase products at high temperatures, diffusing away from the point of ignition in the field of interest promote heat propagation and contribute to an increase in the far-field temperatures. Therefore, a nanothermite that generates greater gas phase products may achieve higher temperatures farther in the field of interest compared to a reaction that does not generate as much gas: a trend that was seen when comparing Al/PTFE and Al/CuO thermal images and temperature profiles.

The variation of maximum temperatures and extend of the temperature fields of the Al/CuO reaction with the addition of metallic nanoparticles shows that the additives have a profound effect on the temperature field. The metallic additives participate in the combustion reaction as additional fuels and react with a solid oxidizer or atmospheric oxygen, releasing heat. Therefore, metallic additives tend to increase $T_{max}$ in the hot region. The amount of chemical energy generated depends on the reactivity of the additives with either of the oxidizers. Table 5 shows heat of combustion for the metal additives and aluminum with oxygen and CuO [28].

Reactions of B and Mg with oxygen and CuO generate the highest heats of combustion, apart from Al as can be seen from Table 5. Since temperature is a measure of the amount of energy present, the same trend is mirrored in the $T_{max}$ values measured from Al/CuO/B and Al/CuO/Mg, as shown in Table 4. On the other hand, Fe and Mn do not react with CuO, even at elevated temperatures, but can oxidize in the presence of oxygen. Therefore, Fe and Mn will need access to atmospheric oxygen which is difficult since

**Table 5.** Heat of combustion values of selected metals on reaction with oxygen and CuO.

| Metal | Heat of combustion on reaction with oxygen [kJ kg$^{-1}$] | Heat of combustion on reaction with CuO [kJ kg$^{-1}$] |
|---|---|---|
| Al | 31023 | 4071 |
| B | 58729 | 3085 |
| Fe | 7373 | no reaction |
| Mg | 26087 | 4606 |
| Mn | 8410 | no reaction |
| Ti | 19704 | 3053 |

  

the composite is a mixture of solid reactants. Thus, it is possible that Fe and Mn may remain condensed phase particles and act as heat sinks. Both Fe and Mn are light weight nanoparticles such that they may also disperse in the combustion cloud and promote an increase in far field temperatures by propagating heat. Such results have been observed when unreactive additives are embedded into pyrotechnic matrices [6,7]. This may be the reason for decreased $T_{max}$ but farther inflection points, when Fe and Mn are added to Al/CuO.

As reported in the results section, the Al/CuO/B and Al/CuO/Mg reactions reached $T_{max}$ much faster than the other nanothermites (see Table 4). It is also seen that the heats of combustion of B and Mg with both CuO and atmospheric oxygen are much greater than with the other additives (see Table 5). In addition, during experimentation the field of interest for Al/CuO/B and Al/CuO/Mg had to be shifted up (from the ignition point to 4 cm above it), implying that the combustion products from these reactions traversed greater distance in a shorter period of time, i.e., they were much faster than the other nanothermites. A direct consequence is that the fast moving gaseous products improved the far-field temperatures due to their high momentum before losing their heat to the environment. Thus Al/CuO/B and Al/CuO/Mg, in addition to having the maximum $T_{max}$ also effectively push their respective inflection points much further away from the ignition point. These observations imply that the temperature fields of the nanothermites may be influenced by the speeds of the reactions.

#### 4.2 Al/PTFE with Metal Oxide Additives

Metal oxides when introduced as additives to Al/PTFE compete with the oxidizer and shift the stoichiometry to fuel lean. This resulted in a general decrease in the $T_{max}$ (see Table 4). However the heat of combustion and the percent gas are relatively constant such that the metal oxide additives effectively shift the inflection point to further distances. Overall, higher gas generation from Al/PTFE aids in dispersion of condensed phase products resulting from the additives and enhances energy propagation in the far-field.

## 5 Conclusions

A unique method for characterizing the temperature fields during the combustion of fast moving energetic materials was developed. Thermal images of Al/PTFE and Al/CuO with and without additives were obtained at the point of time when the reactions reach their maximum temperature. The temperatures were measured using a five channel multi wavelength radiometer coupled with an IR camera. Thermal images show two distinct temperature zones: a *hot zone* surrounding the point of ignition where the highest temperatures ($T_{max}$) were recorded and an intermediate zone, with temperatures lower than those seen in hot zone but much greater than room temperature. Temperature changes along the vertical axis passing through the point of highest temperature were plotted as a function of distance from the point of ignition such that inflection points identifying temperature gradients can be measured to provide an indication of the range of the thermal influence of the reaction.

For Al/CuO, additives with higher heats of combustion like B and Mg increase the maximum temperatures in the hot zone. It was also seen that the faster the reactions attain $T_{max}$ (Al/CuO/B and Al/CuO/Mg), the more extensive the temperature fields generated due to the momentum of the gaseous and condensed phase products, which are ejected farther from the hot zone. This increased the thermal field effects in the far-field regions significantly and shifted the inflection points much farther than the slower moving reactions. Additives like Fe and Mn, produced lower $T_{max}$ and did not react with CuO but showed improved far-field temperatures and farther inflection points as they were more successful in propagating energy from the hot region. Reactions generating more gaseous combustion products like Al/PTFE had increased far-field temperatures and thus farther inflection points compared to reaction that generated less gas like Al/CuO. In addition to the condensed phase products, it was also seen that the gases carried the energy from the hot zone effectively into the far-field. In conclusion, temperature fields are controlled by the introduction of different additives that optimize specific energy transport mechanisms such as overall calorific output coupled with multiphase convection.

## Acknowledgments

The authors are grateful for support from the Army Research Office contract number W911 NF-11-1-0439 and encouragement from our program manager, Dr. Ralph Anthenien.

## References

[1] G. Baudin, A. Lefrancois, D. Bergues, J. Bigot, Y. Champion, Combustion of Nanophase Aluminum in the Detonation Products of Nitromethane, *11th Symposium (International) on Detonation*, Snowmass Village, CO, USA, August 31–September 4, **1998**, p. 989.

[2] K. Balakrishnan, S. Menon, On the Role of Ambient Reactive Particles in the Mixing and Afterburn behind Explosive Blast Waves, *Combust. Sci. Technol.* **2010**, *182*, 186.

[3] V. Boiko, V. Lotov, A. Papyrin, Ignition of Gas Suspensions of Metallic Powders in Reflected Shock Waves, *Combust. Explos. Shock Waves (Engl. Transl.)* **1989**, *25*, 193.

[4] D. Frost, F. Zhang, B. Murray, S. McCahan, Critical Conditions for Ignition of Metal Particles in a Condensed Explosive, *12th Symposium (International) on Detonation*, San Diego, CA, USA, August 11–16, **2002**, p. 693.

[5] P. Haskins, M. Cook, A. Pilgrim, R. Briggs, The Effect of Additives on the Detonation Characteristics of a Lliquid Explosive,

  

*12th APS Topical Group Meeting on Shock Compression of Condensed Matter*, Atlanta, GA, USA, June 28–July 3, **2001**.

[6] W. Thomison, T. Slykhouse, *High Pressure Explosive Compositions and Method using Hollow Glass Spheres*, US Patent 3456589, Dow Chemical Corp., Midland, MI, USA, **1969**.

[7] N. Belov, A. Konyaev, V. Simonenko, A. Stukanov, M. Khabibullin, N. Yugov, Effect of Polymorphous Phase Transformations on Explosive Compression of Steel Spheres, *Combust. Explos. Shock Waves (Engl. Transl.)* **1997**, *33*, 619.

[8] K. Balakrishnan, S. Menon, Characterization of the Mixing Layer Resulting from the Detonation of Heterogeneous Explosive Charges, *Flow Turbul. Combust.* **2011**, *87*, 639.

[9] S. Goroshin, D. Frost, J. Levine, Optical Pyrometry of Fireballs of Metalized Explosives, *Propellants Explos. Pyrotech.* **2006**, *31*, 169.

[10] M. Zachariah, Nanoenergetics: Hype, Reality and Future, *Propellants Explos. Pyrotech.* **2013**, *38*, 7.

[11] N. Yen, L. Wang, Reactive Metals in Explosives, *Propellants Explos. Pyrotech.* **2012**, *37*, 143.

[12] M. Comet, V. Pichot, B. Siegert, F. Schnell, F. Ciszek, D. Spitzer, Phosphorus-Based Nanothermites: A New Generation of Energetic Materials, *J. Phys. Chem. Solids* **2010**, *71*, 64.

[13] H. Miller, B. Kusel, S. Danielson, J. Neat, E. Avjian, S. Pierson, S. Budy, D. Ball, S. Iacono, S. Kettwich, Metastable Nanostructured Metallized Fluoropolymer Composites for Energetics, *J. Mater. Chem. A* **2013**, *1*, 7050.

[14] J. Giles, Collateral Damage, *Nature* **2004**, *427*, 580.

[15] M. Pantoya, J. J. Granier, Combustion Behavior of Highly Energetic Thermites: Nano vs. Micron Composites, *Propellants Explos. Pyrotech.* **2005**, *30*, 53.

[16] M. Pantoya, J. Granier, Laser Ignition of Nanocomposite Thermites, *Combust. Flame* **2004**, *138*, 373.

[17] E. B. Koch, *Metal-Fluorocarbon Based Energetic Materials*, Wiley-VCH, Weinheim, **2011**.

[18] F. Agee, Nanotechnology for Aerospace: Potential Transitions from University Research, *Proceedings of SPIE-International Society for Optical Engineering*, Orlando, FL, USA, April 16–23, **2008**.

[19] E. Nixon, M. Pantoya, G. Sivakumar, A. Vijayasai, T. Dallas, Effect of a Superhydrophobic Coating on the Combustion of Aluminum and Iron Oxide Nanothermites, *Surf. Coat. Technol.* **2011**, *205*, 5103.

[20] S. Grinshpun, A. Adhikari, M. Yermakov, T. Reponen, E. Dreizin, M. Schoenitz, V. Hoffmann, S. Zhang, Inactivation of Aerosolized Bacillus Atrophaeus Endospores and MS2 Virus by Combustion of Reactive Materials, *Environ. Sci. Technol.* **2012**, *46*, 7334.

[21] S. Yan, G. Jian, M. Zachariah, Electrospun Nanofiber based Thermite Textiles and their Reactive Properties, *ACS Appl. Mater. Interfaces* **2012**, *4*, 6432.

[22] K. Martirosyan, Nanoenergetic Gas-generators: Principles and Applications, *J. Mater. Chem.* **2011**, *21*, 9400.

[23] C. Rossi, K. Zhang, D. Esteve, P. Alphonse, Nanoenergetic Materials for MEMS: A Review, *J. Microelectromech. Syst.* **2007**, *16*, 919.

[24] A. Bezmelnitsyn, K. Gangopadhyay, R. Thiruvengadathan, S. Apperson, S. Gangopadhyay, *Nanothermite Based Microsystem for Drug Delivery and Cell Transfection*, Report ADA505079, University of Missouri, Columbia, MO, USA, **2008**.

[25] K. Kappagantula, C. Crane, M. Pantoya, Determination of the Spatial Temperature Distribution from Combustion Products: A Diagnostic Study, *Rev. Sci. Instrum.* **2013**, *84*, 104902.

[26] Y. Shoshin, M. Trunov, X. Zhu, M. Schoenitz, E. Dreizin, Ignition of Aluminum Rich Al-Ti Mechanical Alloys in Air, *Combust. Flame* **2006**, *144*, 688.

[27] Z. Zhang, B. Tsai, G. Machin, *Radiometric Temperature Measurements: Applications*, vol. 2, Elsevier, San Diego, **2009**.

[28] S. Fischer, M. Grubelich, *Theoretical Energy Release of Thermites, Intermetallics and Combustible Metals*, Report SAND95-2448C, Sandia National Laboratories, Albuquerque, NM, USA, **1999**.

Received: October 27, 2013
Revised: April 11, 2014
Published online: May 20, 2014

  